Experimental Study of Inclusion Modification by Ca in AHSS

KEYAN MIAO, MUHAMMAD NABEEL, NESLIHAN DOGAN, and STANLEY SUN

The effects of different Ca and S contents of steel on the modification of endogenous Al_2O_3 inclusions were studied in the laboratory. Three Ca levels (35, 20, 10 ppm) and two S levels (30, 20 ppm) were studied. An automated SEM-EDS system was used for the characterization of inclusions. It was found that the quantity of inclusions in steel increases with the amount of Ca and S contents in the melt. The mechanism of inclusion modification had been discussed based upon the obtained results and thermodynamics. Furthermore, a parameter named 'dimensionless Ca' was introduced, which can be used to estimate the extent of modification of inclusions based upon the Ca content of the steel. This parameter was validated against industrial heats.

I. INTRODUCTION

DEOXIDATION in the ladle is commonly achieved by adding Al in molten steel, but the inevitable formation of Al_2O_3 and $MgAl_2O_4$ spinel inclusions as the deoxidation product is not favourable. These inclusions are not wetted by liquid steel, so they tend to deposit and accumulate inside submerged entry nozzles (SEN) or on a tundish stopper.[1] This triggers nozzle clogging and slows down or even stops the production process. One of the solutions is to modify these inclusions to less detrimental forms. Calcium treatment by powder injection or wire feeding is a common approach used in steel refining to alter the solid Al_2O_3 and $MgAl_2O_4$ inclusions. They react with Ca to form liquid or partially liquid CaO–MgO–Al_2O_3 inclusions,[2–7] so they are less likely to attach onto the refractory lining and stopper when molten steel passes through the nozzle. In addition, modified inclusions are spherical, which helps to avoid steel properties being anisotropic if the shape is maintained after fabricating. Meanwhile, Ca also reacts with dissolved S and forms solid CaS inclusions. This lowers the concentration of dissolved S in steel and minimizes the formation of MnS inclusions. The present study aims to study the fundamentals of Ca interaction with a single oxide, hence focuses only on Al_2O_3.

Total calcium (T.Ca) and total oxygen (T.O) have a significant influence on the type of calcium aluminates that are formed in liquid steel.[8] For example, Yang et al.[9] reported that the Al_2O_3 content decreases drastically when the T.Ca/T.O ratio increases and CaS/CaO ratio in inclusions is linearly related to T.S/T.O. Similarly, Xu et al.[10] reported that CaO content decreases when T.S/T.O increases, and CaS/Al_2O_3 ratio increases with T.Ca/T.O. Based on their calculation, Deng and Zhu[11] proposed that inclusions tend to be $C_{12}A_7$ and C_3A (C and A denote CaO and Al_2O_3, respectively) when T.Ca/T.O ratios are between 0.91 and 1.25. The ratio between Ca and Al was also used to evaluate the calcium treatment results. Sun et al.[1] found the area fraction of Al_2O_3 and CA_6 inclusions and the occurrence of nozzle clogging decreases sharply with T.Ca/ΔAl, where ΔAl = total Al – dissolved Al (T.Al – [Al]). It has also been reported that the amount of steel passing through the tundish nozzle decreases starting when Ca/Al is higher than 0.006 and then increases drastically when Ca/Al is higher than 0.1 when CA forms.[12]

It is suggested that Al_2O_3 is indirectly or directly modified by [Ca] or CaO, and also using transient CaS as the Ca source for modification. Direct modification by [Ca] is believed to be mainly controlled by the transfer of [Ca] in solid Al_2O_3 inclusions.[13–16] Still, a recent study has shown that the mass transport of [Ca] in liquid steel may be the actual primary rate-limiting step.[17,18] Lind and Holappa[19] found that a 5.2 mm CaO cylinder can adequately react with a 3.3 mm Al_2O_3 cylinder within 3 minutes at 1873 K, indicating that the kinetics is fast and modification of micron-sized inclusions will most probably be completed within seconds. The amount of CaO and CaS available for modification

KEYAN MIAO, MUHAMMAD NABEEL, and NESLIHAN DOGAN are with the McMaster University, Faculty of Engineering, 1280 Main Steet West, Hamilton, ON L8S 4L8, Canada. Contact e-mail: miaok@mcmaster.ca STANLEY SUN is with the ArcelorMittal Global R&D - Hamilton, 1390 Burlington Street East, Hamilton, ON L8H 3N8, Canada.

was suggested to be dependent on [O] and [S] concentrations, which determine the probability of them occupying a CaO or CaS nucleation site on the Ca gas–liquid surface.[20,21] Previous studies[10,21–28] focused on determining the sequence of reactions between inclusions and calcium, minimizing the mass of calcium addition while promoting the formation of calcium aluminate inclusions, and controlling the formation of CaS inclusions. Some researchers[17,19,23,29] also focused on the kinetics of transformation between inclusion phases. However, due to the nature of a complex multi-component system and vigorous reactions at high temperatures, a significant amount of uncertainties occur during the experiments and industrial practices. Therefore, despite a wide range of steel conditions that have been considered, there is no established reaction mechanism to explain the modification of inclusions. In addition, despite findings and theories related to the Ca treatment process have been reported, an accessible indicator of proper calcium treatment for industrial practice is still absent in the literature.

The present research aims to understand the effect of Ca addition on the modification of inclusions in liquid steel. Based on the results of laboratory experiments, an inclusion modification mechanism is proposed to explain the details of inclusion evolution. Thermodynamic calculations, Ca addition experiments, and SEM-EDS analysis are used for this purpose. By the end, the amount of Ca addition to the specific steel chemistries has been suggested.

II. EXPERIMENT METHODOLOGY

Inclusion modification experiments were conducted in a vertical tube furnace at 1873 K. A schematic diagram of the experimental setup is shown in Figure 1. To prepare the synthetic melt, about 6.5 g Mn (from Alfa Aesar), 0.3 g graphite rod (from McMaster-Carr), and 0.027 or 0.04 g FeS (from Fisher Scientific) were initially added to the electrolytic iron (from North American

Höganäs). The total mass of the synthetic melt was 500 g. The composition of steel will be discussed in a later section. All base materials held within an Al_2O_3 crucible (inner diameter 5.6 cm, height 10.4 cm) was placed in the hot zone of the furnace and heated to 1873 K. Al_2O_3 crucibles were used instead of MgO or CaO. The purpose was to prevent the formation of spinel inclusions due to reaction with MgO crucible and the effect of CaO crucible on Ca content of the steel. Ar gas with 99.999 pct purity was fed continuously into the furnace at a rate of 0.5 L/min after passing through Ti turnings at 973 K to maintain a protective atmosphere. The oxygen was continuously measured by an oxygen sensor connected to the gas outlet of the furnace. The partial pressure of oxygen was measured to be about 10^{-16} atm during the experiment.

The course of a representative modification experiment is shown in Figure 2. The crucible was heated from room temperature to the experimental temperature of 1873 K at a rate of 10 K/min, then held for 30 minutes to homogenise the liquid steel. Thereafter, Al and Si were added simultaneously through the feeding/sampling tube to achieve 0.03 and 0.25 pct content in steel, respectively. After 15 minutes, Ca was added to the molten steel. This is considered as the time-zero of all modification experiments. Pin-shaped samples (5 mm diameter, 10 cm length) were then taken at different holding times before and after Ca addition. In all experiments, Al and Si were introduced in the form of small lumps, while Ca was wrapped in steel foils together with some electrolytic Fe. The use of a small pin sample instead of the ASTM cleanliness evaluation standard is that a smaller sample preserves more high temperature inclusions due to its relatively faster cooling rate.[30] Assuming that a pin sample is a lumped system, the estimated cooling rate of pin samples in the air is about 2.5 K/s.

Steel samples were used to analyse steel chemistry and the characteristics of inclusions. Both ends of a pin sample were removed before chemical analysis. After that, the oxide scale on the pin sample surface was removed to avoid its influence on the chemical analysis. The chemistry of the steel samples was determined using inductively coupled plasma optical emission spectrometry (ICP-OES) and LECO™ CS744 carbon/sulfur analyzer. LECO™ ON736 oxygen/nitrogen analyzer was used to measure the total oxygen (T.O) content for some samples. Accuracy of concentrations was also confirmed against results obtained through the spark OES-PDA (Pulse height Distribution Analysis) method. T.O was not measured in some experiments due to an insufficient amount of sample.

A section of the pin sample was cut along the longitudinal axis to expose the centre for inclusion analysis. The samples were first ground using SiC of 120 to 1200 grit. Ethanol was used as the lubricant during this process to avoid any potential reaction with Ca. Samples were then sequentially polished by using water-free diamond suspension containing 6, 3, and 1 μm average particle size. An automated SEM-EDS system (ASPEX) was employed to observe and characterize inclusions on the polished cross-sections. The
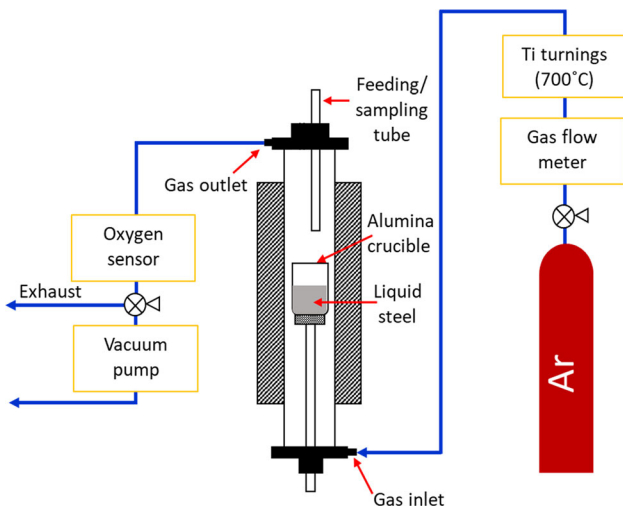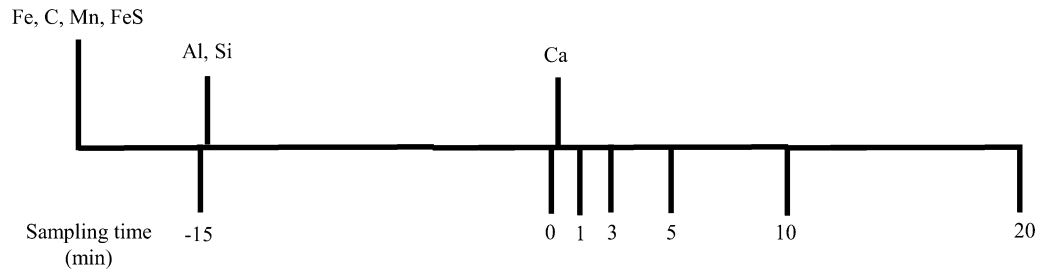

Fig. 1—Schematic diagram of the experimental setup.

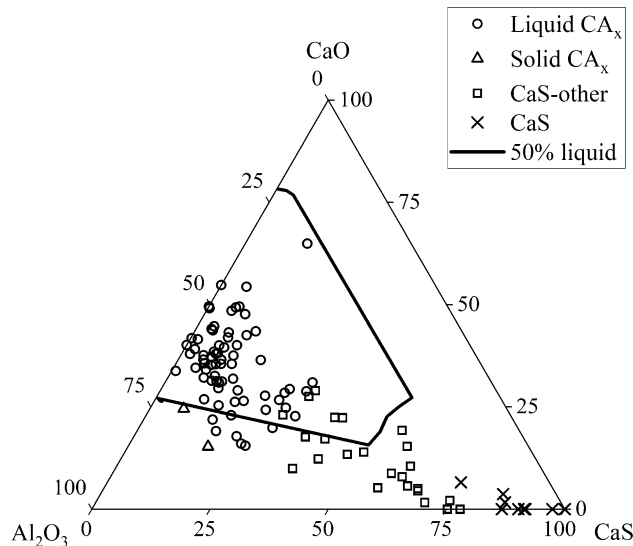Fig. 2—Flow chart of a typical inclusion modification experiment.

Fig. 3—Inclusion distribution represented on a ternary diagram from Exp. 3020 at 20 min after Ca addition. A solid line illustrates 50 pct liquid region.

analysed cross-section area varied from 10 to 40 mm^2. In the current study, the inclusions having a maximum diameter (D_{max}) larger than 2 μm were considered for analysis. Smaller inclusions were not considered because they are considered less detrimental. Moreover, inclusions with an average diameter larger than 5 μm and features with irregular shapes were also not considered in the analysis due to their negligible percentage.

ASPEX conducted an EDS analysis on every detected inclusion. Based on the results, the detected inclusions were classified into seven types: Ca-rich, liquid CA$_x$, solid CA$_x$, CaS, CaS-other, CaS-MnS, and MnS. Liquid CA$_x$ includes low melting point C$_3$A, C$_{12}$A$_7$, and CA inclusions, whereas solid CA$_x$ includes high melting point CA$_2$ and CA$_6$ inclusions. Ca-rich inclusions are inclusions with higher CaO content than the liquid CA$_x$. CaS-other inclusions are those with compositions between CaS and CA$_x$. CaS–MnS inclusions have a significant fraction of both CaS and MnS; however, their fractions are not high enough to be considered as a single-phase CaS or MnS. Figure 3 shows the distribution of inclusion types detected in a sample from Exp. 3020 (meaning explained in the next section) at 20 minutes after Ca addition as an example. The CaO–Al$_2$O$_3$–CaS ternary diagram is represented based on

weight fraction. The region bounded by a solid line represents the 50 pct liquid region at 1873 K calculated using FactSage. As can be seen, the inclusion types cover corresponding areas of the diagram. Liquid and solid CA$_x$ are inside and outside the 50 pct liquid region, respectively. CaS inclusions are close to the CaS corner, and CaS-other inclusions lie between CaS and CA$_x$. In some cases, the areas of two types overlap on the graph, but generally, the change of inclusion types between samples corresponds well with the shift in inclusion compositions. Therefore, inclusion types are used instead of detailed compositions in most of the following contexts for simplicity.

III. EXPERIMENTAL RESULTS

A. Steel Chemistries

In this study, six experiments were conducted, which can be divided into two sets. In the first set, three different amounts of Ca (*i.e.*, ~ 1.2, 0.8 and 0.4 g) were added in a 500 g experimental steel containing 20 ppm S. Whereas, in the second set a 30 ppm S containing steel was treated with Ca levels similar to that in the first set. The detailed composition of all experimental steels is shown in Table I. The error of Ca and S contents are based on two standard deviations of repeated measurements to give 95 pct confidence. The experiments are denoted in the form of "[S content][Ca content]". Here the Ca content of samples taken after 20 minutes of Ca addition is used. For example, Exp. 2035 represents the experimental condition with 20 ppm S and 35 ppm Ca. Deriving from this format, 2035-*X* is used to describe a sample obtained at *X* minutes after Ca addition in Exp. 2035.

For all experiments, Si and C contents didn't vary during an experiment and kept constant at about 0.25 and 0.06 wt pct, respectively. Similarly, the Mn content remained stable at close to 1 pct, except for Exp. 2020 where Mn content was measured to be about 0.75 wt pct.

In all experiments, the Al content was estimated to be 0.03 wt pct in the samples taken after adding Al and before Ca addition. During the experiment, the reaction between Ca and Al$_2$O$_3$ crucible increased dissolved Al in the system (Reaction (1)). Due to this reason, the Al content increased within 1 minute after Ca addition, as indicated in Table I, then remained constant throughout the experiment. The increments are in positive correlation with Ca content.

Total Ca concentration (T.Ca) generally decreased over time, especially in Exp. 2035 and Exp. 3020, which had about 20 ppm Ca drop. Whereas in Exp. 2010 and Exp. 3010, T.Ca remained nearly constant. The decrease in T.Ca is likely due to Ca evaporation and reaction with the crucible. The Ca-crucible reaction is indicated by the increased Al and O contents of steel after Ca addition, as well as the fact that calcium aluminates (CA_x, here C and A denote CaO and Al_2O_3, respectively) were found on the crucible inner wall. SEM images of the crucible inner surface before and after the experiment are shown in Figure 4. As shown in Figure 4(a), the crucible generally had homogeneous Al_2O_3. After a modification experiment, multiple new phases appeared on the crucible inner surface (Figure 4(b)). According to the EDS measurement, Ca concentration gradually decreased from about 15 wt pct at the inner surface (CA_x phase 1) to 9.5 wt pct in the middle (CA_x phase 2) then 4 pct in a layer adjacent to the crucible body (CA_x phase 3). The crucible body after the experiment contained about 1 wt pct Ca.

B. Inclusion Compositions and Quantities

Figure 5 presents the variation in the area fraction (AF) and the number per unit area (N_A) of all inclusions observed in each experiment. Area fraction was calculated as the area of inclusions divided by the area of steel matrix scanned in ASPEX. As can be seen in Figure 5(a), for all the experiments, a similar value of total AF (about 13E-6) was found in the sample taken before Ca addition. Just after Ca addition, the AF value decreased and then gradually increased till the end of the experiment. It can also be seen that a higher T.Ca led to a higher AF of inclusions. This tendency can be clearly seen by comparing the AF of inclusions in samples taken after 20 minutes of Ca addition. Exp. 2035 had almost ~ 13 times higher AF than that of Exp. 2020. Similarly, for 30 ppm S set experiments, the AF of inclusions in 35 ppm Ca containing steel (Exp. 3035) was ~1.6 and ~16 times of the AF of inclusions in Exp. 3020 and Exp. 3010, respectively. The evolution of N_A is presented in Figure 5(b), which exhibits similar trends to those of the AF change in Figure 5(a). Hereafter, the AF of inclusions is used to present and discuss the results. According to Table I, no significant T.O and T.S content changes were observed in any experimental heats other than Exp. 2010, in which the AF increase was negligible. Therefore, a significant AF growth seen in Figure 5 cannot be attributed to T.O or T.S change. The fact that AF increase was more apparent in high Ca experiments suggests that undetected tiny CaS inclusions formed in early stages, their size increased with time either through particle coarsening or agglomeration, and then became detectable by ASPEX.

Figure 6 presents the AF variation of the main types of inclusions observed in experimental steel. Apart from these types, a neglectable amount (< 5 pct of total inclusions) of Ti and Mg containing inclusions was detected.

In Exp. 2035 (Figure 6(a)), Ca-rich inclusions appeared just after Ca addition, and their AF remained almost constant (at about 4 ppm) until 10 minutes. CaS inclusions appeared in the sample taken at 3 minutes after Ca addition, and the AF of these inclusions increased from 0.5 to 44 ppm till 20 minutes. A tiny amount (0.8 ppm) of liquid CA_x appeared in 10 minutes sample, which substantially increased to 5.7 ppm in the sample taken after 20 minutes of Ca addition. CaS-other inclusions started to emerge from the beginning of this experiment; however, the AF only became significant in 20 minutes sample.

With a less Ca addition, Exp. 2020 (Figure 6(b)) did not exhibit any considerable AF of Ca-rich inclusions. Instead, liquid CA_x and CaS appeared within 1 minute after Ca addition. After that, the AF of liquid CA_x remained almost constant (at ~ 0.6 ppm) in the first 10 minutes and then increased to 2.9 ppm in 20 minutes sample. In comparison, the AF of CaS decreased to a relatively low amount in 20 minutes. From 2020-1 to 2020-5, the AF of CaS-other inclusions increased from 0.05 ppm to 0.9 ppm, then slightly decreased to 0.8 ppm at 20 minutes.

As Ca addition further decreased, in Exp. 2010 (Figure 6(c)), the retention of Al_2O_3 inclusions shortly after Ca addition was observed. Another feature of the Exp. 2010 was the appearance of CaS–MnS and MnS. Although their AF were still incomparable to any other major inclusion types, their existence indicated the modification results were different from the other two experiments shown above.

Unlike 20 ppm S containing steel, a higher Ca addition in 30 ppm S containing steel (i.e. Exp. 3035) didn't produce Ca-rich inclusions (compare Figures 6(a) and (d)). Instead, 2.3 ppm liquid CA_x and 4.1 ppm CaS inclusions were observed in Exp. 3035 just after Ca addition and the AF of liquid CA_x and CaS gradually increased to 9.4 ppm and 22.1 ppm during the experiment, respectively. However, by the end of 20 minutes, the inclusion characteristics of Exp. 3035 were very similar to those of Exp. 2035, except with less CaS relative to CA_x in Exp. 3035.

In Exp. 3020 (Figure 6(e)) the AF of liquid CA_x and CaS inclusions increased with holding time. Between 1 and 20 minutes, the AF of liquid CA_x increased from 0.4 to 15.5 ppm. Also, the AF of CaS-other and CaS inclusions gradually increased from 0.7 to 4.8 and 0.5 to 1.9 ppm, respectively. Moreover, CaS-MnS and MnS inclusions were detected throughout the experiment with a small AF.

The inclusion characteristics in Exp. 3010 (Figure 5(f)) were similar to those of Exp. 2010 (Figure 5(c)). The similarity came from two key characteristics. First, the oscillating AF of Al_2O_3. Exp. 3010 and Exp. 2010 were the only two cases with Al_2O_3 being formed after Ca addition. The other feature was the increase in the AF of CaS inclusions from 0.5 to 1.1 ppm followed by decreasing to 0.4 ppm. Except for the AF of CaS in Exp. 3010 was generally higher than that in Exp. 2010.

| Exp. #	2035	2020	2010	3035	3020	3010
	Ca (ppm)					
Time (min)						
1	56 ± 3	29 ± 3	10 ± 3	42 ± 1	37 ± 1	15 ± 2
3	50 ± 2	20 ± 2	11 ± 3	41 ± 1	19 ± 2	14 ± 2
5	48 ± 2	17 ± 2	11 ± 3	40 ± 1	17 ± 2	14 ± 2
10	46 ± 4	20 ± 2	10 ± 3	39 ± 1	17 ± 2	N/A
20	37 ± 3	18 ± 3	9 ± 3	37 ± 1	17 ± 2	13 ± 2
	S (ppm)					
1	21	22	18	31	32	25
3	23	22	18	32	33	26
5	23	22	18	30	32	31
10	26	23	18	27	34	26
20	21	23	19	34	33	25
	Al (wt pct)					
1	0.1	0.039	0.037	0.059	0.055	0.041
3	0.090	0.042	0.034	0.062	0.056	0.041
5	0.093	0.041	0.041	0.061	0.055	0.042
10	0.096	0.042	0.036	0.062	0.052	N/A
20	0.090	0.051	0.036	0.062	0.056	0.043
	O (ppm)					
0	21	25	23	n/a	21	n/a
1	25	12	14	n/a	13.2	n/a
3	22	18	37	n/a	11	n/a
5	24	23	45	n/a	14	n/a
10	35	31	7	n/a	40	n/a
20	30	29	n/a	n/a	23	n/a
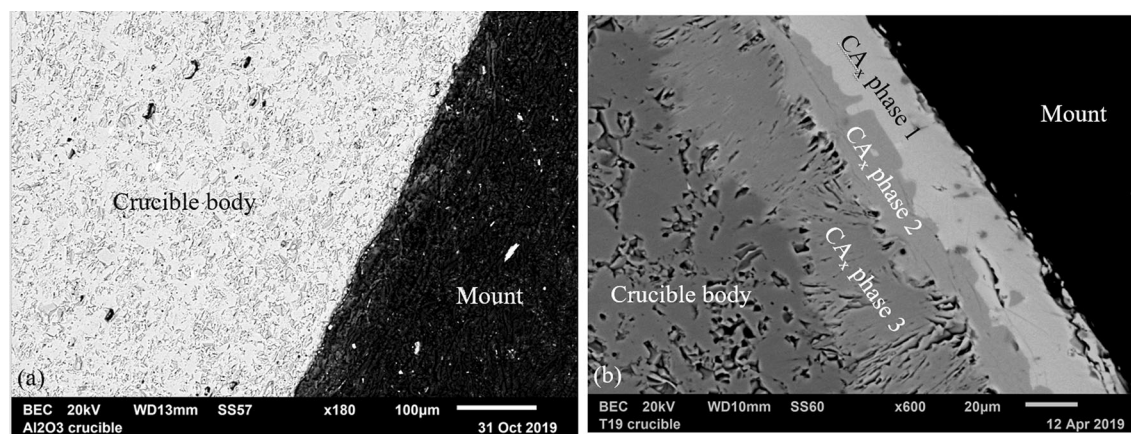
Fig. 4—A typical SEM backscatter image of the Al_2O_3 crucible (*a*) before and (*b*) after an experiment.

IV. DISCUSSION

A. *Effect of Ca and S Contents on Inclusion Stabilities*

Thermodynamic calculations were carried out by employing Factsage 7.2 to predict stable phases in molten steel at 1873 K. The stability diagram of inclusions in experimental steel containing 20 ppm and 30 ppm S are shown in Figures 7(a) and (b), respectively. Based upon the measured T.O values, a value of 20 ppm was used in these calculations.

Figure 7 shows that CaO, CaS, liquid CA_x, and CA_2 are in equilibrium with molten steel containing 5 to 60 ppm Ca and 0.03 to 0.1 pct Al. The inclusion stability mainly varies with Ca content. While liquid CA_x is
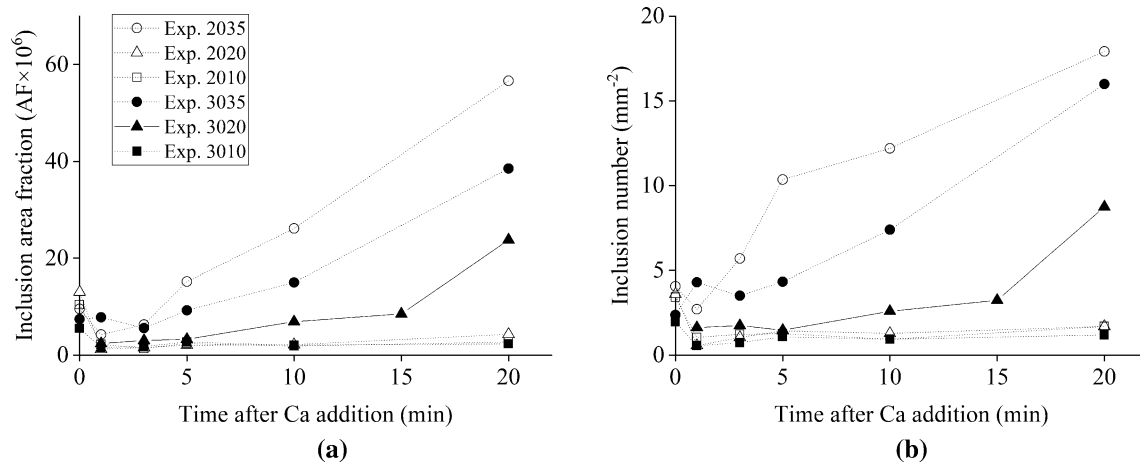
Fig. 5—Inclusions quantity evolution from six experiments studied in the form of (*a*) area fraction (AF) change and (*b*) number (N_A) change.

always stable, decreasing Ca leads to the disappearance of thermodynamically stable CaO, then CaS, and finally the formation of CA_2. CaS stability is associated with S content. By increasing S content from 20 to 30 ppm, the CaS stable region expands by narrowing both liquid CA_x and CaO stable regions. However, the formation of liquid CA_x and CA_2 does not depend on S content; hence, it appears identical in Figures 7(a) and (b).

Hollow marks in Figure 7 represent the measured Ca and Al contents of samples taken after Ca addition. The sampling sequence has been shown in detail in Table I. Inclusion stability diagrams show that regardless of S content, the samples from higher Ca addition experiments (Exp. 2035 and Exp. 3035) lied above the fully liquid region. Moreover, for Exp. 2035, the samples taken within 10 minutes of Ca addition were in the CaO stability region. This explains the presence of Ca-rich inclusions in Exp. 2035 and a substantial amount of CaS inclusions in both Exp. 2035 and Exp. 3035. Exp. 2020 and Exp. 3020 had initial compositions located in the region where CaS is stable, and as the Ca content stabilized, both experiments ended in the fully liquid region. The inclusion analysis also shows that the majority of the inclusions in these two experiments were liquid CA_x. All the samples from Exp. 2010 lied close to the CA_2 saturation line. Whereas, those of Exp. 3010 were in the fully liquid region. As mentioned earlier, the equilibrium line between liquid CA_x and CA_2 is independent of S content. The different locations of Exp. 2010 and Exp. 3010 are due to the slight variation in their Ca contents (see Table I). This difference, to some extent, does reflect on the modification results.
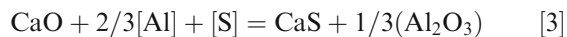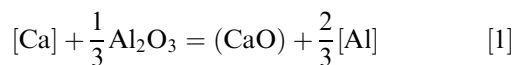
B. Effects of Ca and S Contents on Modification Mechanism

An occurrence of Ca-rich (mainly CaO) inclusions in Exp. 2035 (see Figure 5) suggests that the inclusions modification mechanism for this experiment is different than that of the other five experiments. The following discusses the possible inclusion modification mechanisms involved in all the experiments conducted in the current study.

1. Mechanism involving CaO inclusions

When Ca is added to molten steel, due to its volatile nature, it can leave the system in the form of gas, and some of it can dissolve in molten steel as [Ca]. [Ca] is consumed in three ways: (1) reduction of the Al_2O_3 inclusions in accordance with Reaction (1) (CaO in round brackets denotes CaO and Al_2O_3 are miscible); (2) formation of CaS according to Reaction (2); and (3) reaction with Al_2O_3 crucible. Reaction (1) is considered as a primary route of CaO formation since ASPEX did not detect visible AF of Al_2O_3 inclusions in sample 2035-1, as seen in Figure 6(a).

$$[Ca] + \frac{1}{3}Al_2O_3 = (CaO) + \frac{2}{3}[Al] \qquad [1]$$

$$[Ca] + [S] = CaS \qquad [2]$$

$$CaO + 2/3[Al] + [S] = CaS + 1/3(Al_2O_3) \qquad [3]$$

In addition to the formation of CaS by Reaction (2), Ca-rich inclusions transform to CaS inclusions following Reaction (3). During the transformation from Ca-rich inclusions to CaS, CaO reacts with [Al] to form Al_2O_3 as part of CA_x (denoted using round brackets). This can be confirmed by their chemistry change. By using the method described by Lind and Holappa,[19] elemental compositions of inclusions obtained by EDS during ASPEX analysis can be converted to mass fractions of MnS, CaO, Al_2O_3, and CaS. The compositions of CaS and Ca-rich inclusions at different times in Exp. 2035 are plotted in Figure 8. MnS is not included as it is considered as a solidification product that does not exist at 1873 K. Although these inclusions are
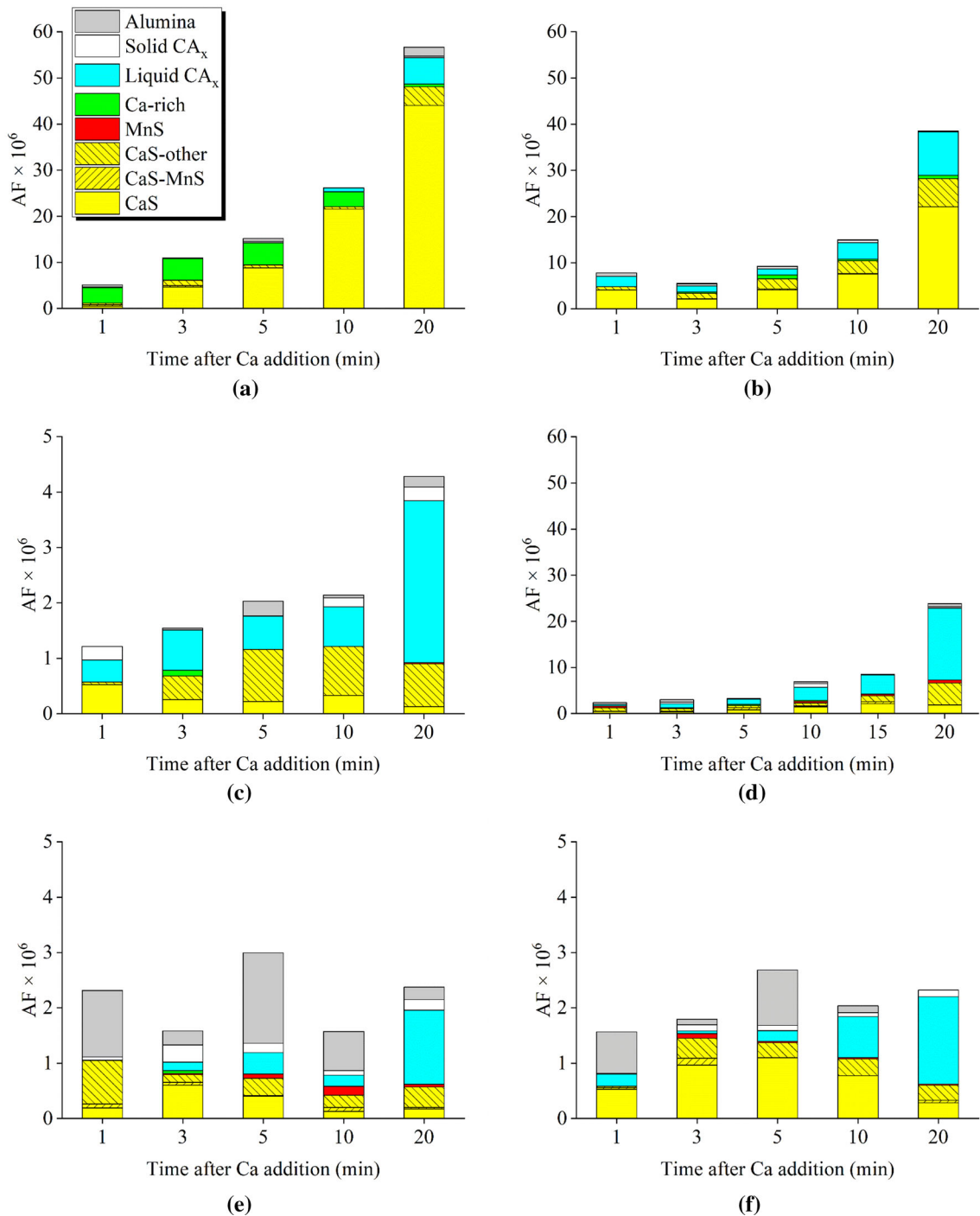
Fig. 6—Evolution of inclusion area fraction (AF) in (*a*) Exp. 2035, (*b*) Exp. 2020, (*c*) Exp. 2010, (*d*) Exp. 3035, (*e*) Exp. 3020 and (*f*) Exp. 3010.

classified as "CaS" and "Ca-rich" in the inclusion analysis, they are all CaO–CaS complexes. Before 10 minutes after Ca addition, the complexes were almost composed of only CaO and CaS (Figures 8(a) through (c)). As the experiment proceeded, Ca-rich and CaS became richer in CaS, and at 20 minutes, the fraction of Al_2O_3 increased. Therefore, the respective increase and decrease of CaS and Ca-rich AF shown in Figure 6 reflect a continuous CaO to CaS transformation in CaO-CaS complexes throughout the experiment

according to Reaction (3). CaS can also be a solidification product due to its increased stability at lower temperature.[20,31] However, these inclusions most probably have sizes under the detection limit of ASPEX with the short solidification time in pin samples.

EDS mappings on Ca-rich inclusions were also performed to verify the occurrence of early CaO to CaS transformation. Examples of two such inclusions are shown in Figure 9. The elemental map of Ca in both inclusions cover almost the entire inclusions surface,
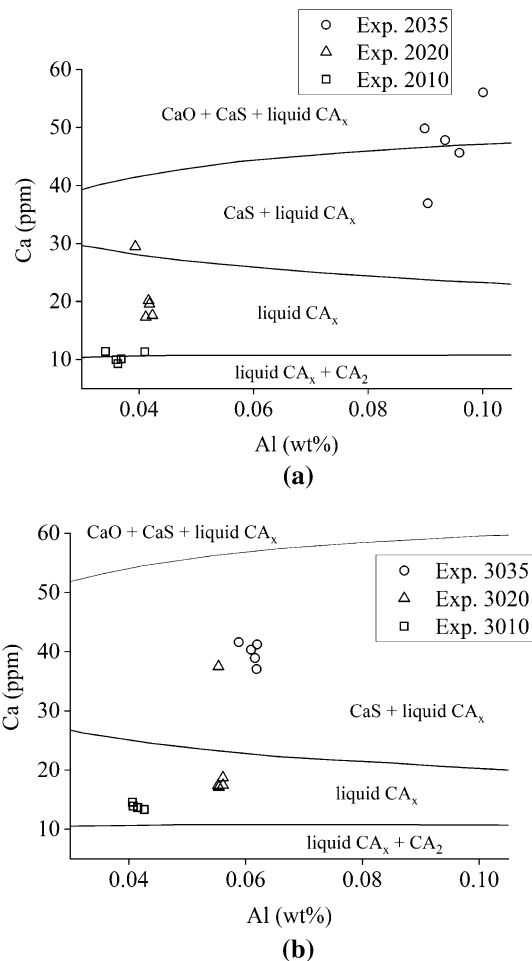
Fig. 7—Inclusion stability diagram constructed using FactSage for experimental steel containing (*a*) 20 ppm S and (*b*) 30 ppm S and constant 0.06 wt pct C, 0.25 wt pct Si, 1 wt pct Mn and 20 ppm T.O.

while the map of S misses some region as the upper part of the inclusions in Figures 9(a) and (b). Even though the low contrast in O maps causes some difficulty to directly compare with S and Ca maps, both inclusions in Figure 9 are likely CaO–CaS dual-phase inclusions.

After the CaO to CaS transformation, CaS becomes the main Ca bearer, hence is the major Ca source for oxide modification. These Al_2O_3 inclusions are modified by CaS in accordance with Reaction (4). In this case, CaO is not the major Ca source for modification through Reaction (5) because the concentration of [Ca] and CaO were low after Reaction (3).

$$3CaS + (Al_2O_3) = 3(CaO) + 2[Al] + 3[S] \qquad [4]$$

$$xCaO + yAl_2O_3 = xCaO \cdot yAl_2O_3 \qquad [5]$$
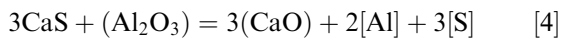
2. *Mechanism in the absence of CaO inclusions*

Similar to Exp. 2035, the added Ca in all the other experiments participated in reducing Al_2O_3 inclusions, the formation of CaS, and reacting with Al_2O_3 crucible. However, due to low Ca content and thermodynamic instability, CaO (Ca-rich inclusion) was not formed, but instead, Reaction (1) resulted in the formation of CA_x. The occurrence of liquid CA_x within 1 minute of Ca addition is in agreement with the suggestion of Tabatabei *et al.*,[17] *i.e.*, the transformation of micron-sized Al_2O_3 to liquid CA_x can complete in a very short time. In all the experiments, CaS or CaS-other inclusions were formed immediately after Ca addition.

The [Ca] is consumed immediately after Ca addition resulting in the formation of liquid CA_x and CaS containing inclusions. Any further modification will use CaS as the Ca source (Reaction (4)). Unlike the aforementioned [Ca]–Al_2O_3 reaction, modification of Al_2O_3 by CaS involves two solids, which is understandably slower than [Ca]–Al_2O_3 modification reaction. Hence, a detectable amount of oxysulfide inclusions as reaction intermediates is likely to exist. CaS-other inclusions were defined in ASPEX inclusion classification to be oxysulfide complexes compounded by a similar amount of CaS and Al_2O_3 or CA_x. They may be the reaction intermediates of Al_2O_3 or CA_x modified by CaS.

The SEM-EDS elemental maps of some typical oxysulfide inclusions are shown in Figure 10. All four inclusions exhibit two separate phases. In Figures 10(a) and (b), Ca, and S elemental maps overlap and correspond to the upper and left region of the inclusions, respectively. In Figure 10(b), some Ca was also detected in the right part of the inclusion. Al and O maps cover the lower and right part of these inclusions. This implies that Figure 10(a) likely shows a CaS–Al_2O_3 complex inclusion, whereas Figure 10(b) is an CaS–CA_x complex inclusion. Similar inclusions can also be found at 20 minutes after Ca addition as shown in Figures 10(c) and (d).

The variation in the composition of CaS-other inclusions with time is shown in Figure 11 for all the experiments except Exp. 2035. It can be seen that for all the experiments, the mass fraction of CaO + Al_2O_3 increased from less than 50 wt pct to around 60 wt pct, while that of CaS decreased from more than 50 wt pct to approximately 40 wt pct. The EDS mapping presented in Figure 9 and the variation in the composition of CaS-other inclusions shown in Figure 10 supports the suggested modification mechanism of inclusions modified by CaS.

In the present study, the amount of MnS inclusions formed is directly related to [S] because [Mn] levels are similar across experiments and sample cooling rates are assumed to be similar. The formation of MnS and CaS-MnS inclusions was observed in Exp. 2010, Exp.
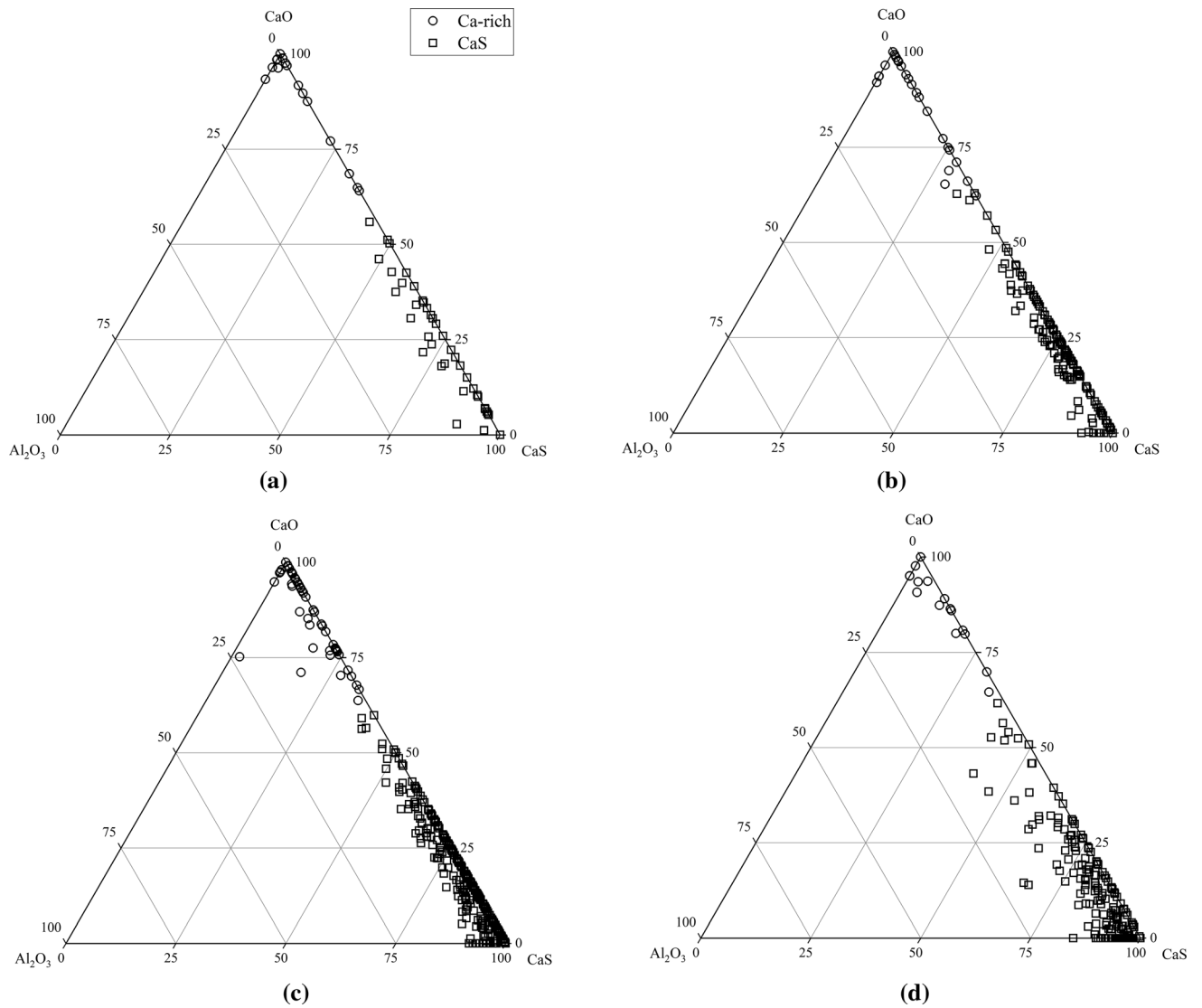
Fig. 8—CaO, Al$_2$O$_3$ and CaS mass fractions of Ca-rich and CaS inclusions in Exp. 2035 at (*a*) 1 minute (*b*) 5 minutes (*c*) 10 minutes and (*d*) 20 minutes after Ca addition.
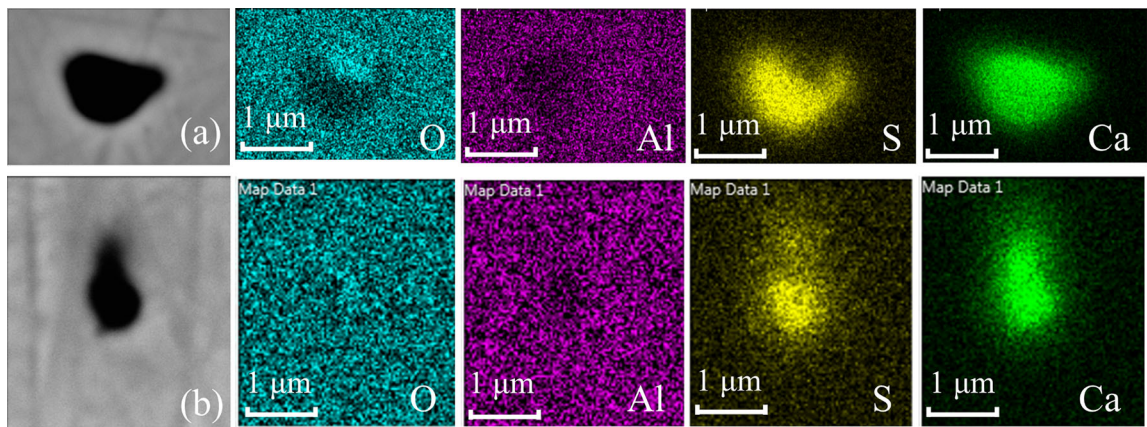

Fig. 9—SEM-EDS elemental maps of CaO-CaS dual-phase inclusions from Exp. 2035 samples (*a*) and (*b*) both taken at 3 minutes after Ca addition.
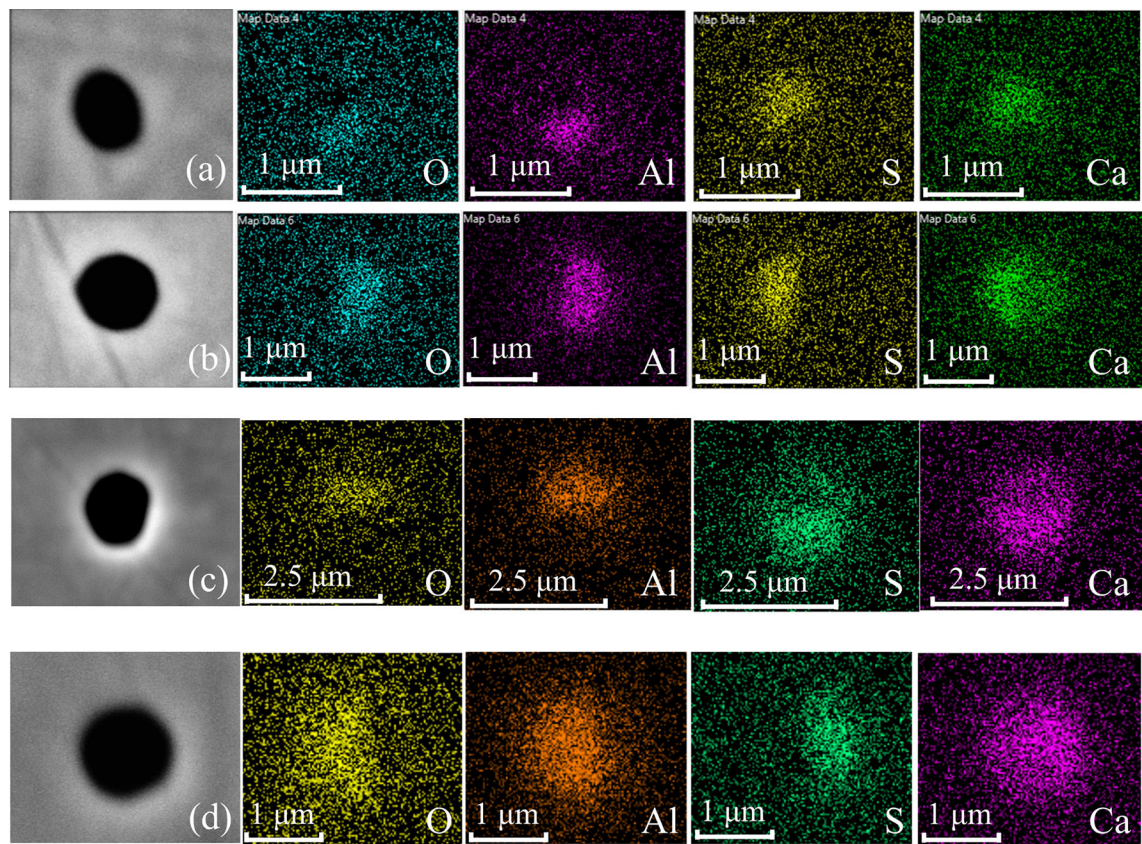
Fig. 10—SEM-EDS elemental maps of typical oxysulfide inclusions observed in the sample taken at (*a*) and (*b*) 3 minutes after Ca addition (*c*) and (*d*) 20 minutes after Ca addition in Exp. 2020.
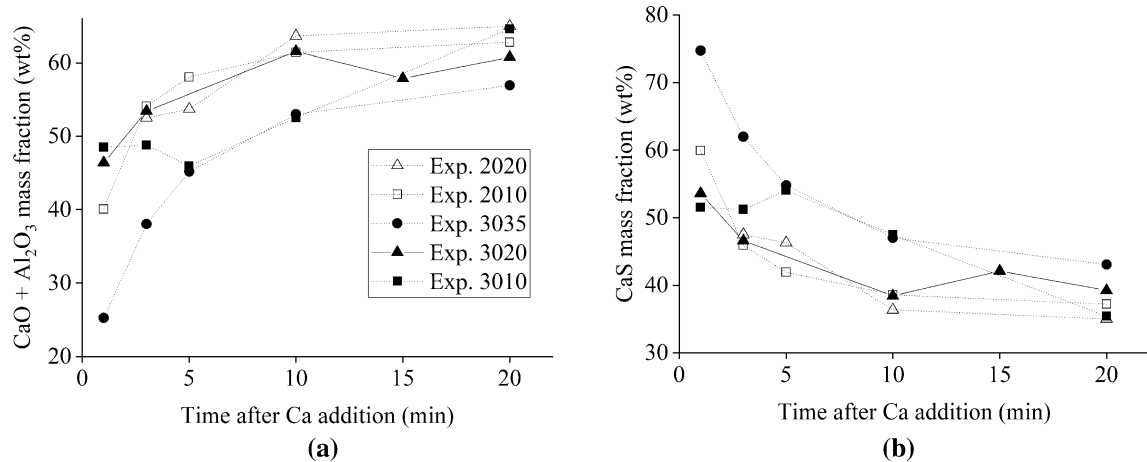

Fig. 11—Change of CaS-other average compositions (*a*) CaO + Al$_2$O$_3$ (*b*) CaS in Exp. 2020, Exp. 2010, Exp. 3035, Exp. 3020 and Exp. 3010.

3020 and Exp. 3010. Due to either the low Ca content or high S contents, these experiments still had sufficient [S] to precipitate MnS during solidification.

Based upon the discussion in the above section, the inclusion modification mechanism for the current experimental steel compositions can be summarized as below:

1. [Ca] in liquid steel reduces Al$_2$O$_3$ and depending on the amount of added Ca, the reaction product could be CaO or different types of CA$_x$ (or remains Al$_2$O$_3$ in the case of low Ca additions). At the same time, [Ca] desulfurizes liquid steel to produce CaS.
2. In the case where CaO is formed, CaO gradually reacts with [S] to produce CaS and [O]. The produced

[O] reacts with [Al] to form Al_2O_3, which is modified to CA_x by CaS.

3. With low Ca addition, the inclusions are CA_x (and potentially some Al_2O_3) and CaS. CaS is now the only Ca source. Hence, CaS will further modify CA_x to a higher modification extent.

4. If the conditions (mainly [S]) satisfy the criteria of MnS nucleation or precipitation, MnS and CaS-MnS inclusions will form during solidification.

V. COMPARISON OF MODIFICATION RESULTS

From the perspective of improving castability, liquid and semi-liquid inclusions are preferred. The samples taken at 20 minutes after Ca addition are selected to compare the extent of liquefication achieved in each experiment. The AF of different types of inclusions at 20 minutes after Ca addition is normalized to 100 pct and shown in Figure 12(a). The exact AF values are already shown in Figure 6. The three high CaS inclusion types, CaS, CaS-other and CaS-MnS are more than 70 pct of the overall inclusion AF in Exp. 2035 and Exp. 3035. In the other four experiments, the percentages are about 20 pct. The excessive CaS formation indicates over-modification in the two 35 ppm Ca experiments. The liquid CA_x percentages appear similar in 20 and 10 ppm T.Ca experiments regardless of S content, but are in fact, very different as types of CA_x formed vary. Figure 12(b) shows the relative area fraction of CA_x inclusions. The

Fig. 12—Normalized AF of (*a*) all inclusions and (*b*) CA_x inclusions in six experiments at 20 minutes after Ca addition.

CA_x presented in 20 minutes samples of Exp. 2035 and Exp. 3035 were highly modified as more than 80 pct of their AF contains C_3A and $C_{12}A_7$. However, since the amount of CaS was significant (6 times more than AF of all CA_x), these experiments are not considered to have superior modification results. The liquid CA_x (CA + $C_{12}A_7$ + C_3A) had the highest percentage of AF (> 60 pct) among all inclusion types in the other four experiments. However, according to Figure 12, the CA_x from Exp. 2010 is less modified compared to those of Exp. 2020, Exp. 3020 and Exp. 3010. This is because about 68 pct of the CA_x in Exp. 2010 were CA, and the melting point of CA is very close to 1873 K. If the same inclusion combination appears in the industrial heats at a lower temperature, the castability may still be negatively affected. The steel compositions of Exp. 2020, Exp. 3020 and Exp. 3010, with at least 28 pct CA_x being $C_{12}A_7$ and limited CaS, exhibited preferred modification results. This agrees with the thermodynamic calculation presented in Figure 6, which shows that the endpoint Ca contents of these three experiments felt in the liquid CA_x region.

As inferred from Figure 12, a comparison of AF of CA_x inclusions can help determining a relative modification extend of specific steel chemistries as compared to that of others. However, the AF of CaS containing inclusions must also be considered when adopting the idea of Figure 12. Moreover, this idea of determining the extent of modification counts on inclusion analysis, which can't be conducted on-line during the production of a heat. Therefore, it is necessary to have a parameter that can be determined on-line and can also hint at the extent of modification of inclusions. For this purpose, Sun *et al.*[1] proposed a parameter called Ca treatment index. It is a ratio between Ca content of steel and the Al content present in the form of inclusions (Al_{inc}). Hence, the authors propose a new parameter that can be used to estimate the extent of inclusion modification by correlating thermodynamics and measured Ca content of the steel. For this, the measured Ca content of steel and inclusion stability diagrams (given in Figure 7) are used to determine the location of measured Ca content in the liquid window (liquid CA_x region) of the stability diagram. The site is determined relative to the two boundaries (CA_2 saturation line and CaS saturation line) of the liquid window for the steel composition of interest. This relative location measured Ca content on the stability diagram is named as dimensionless Ca, and can be calculated using Eq. [6]. Where, $(T.Ca)_{measured}$, $(T.Ca)_{CA_2sat.}$ and $(T.Ca)_{CaSsat.}$ are the measured T.Ca, T.Ca required for CA_2 saturation and T.Ca required for CaS saturation, respectively. $(T.Ca)_{CA_2sat.}$ and $(T.Ca)_{CaSsat.}$ are calculated by determining the functions of the CA_2 saturation line and CaS saturation line on the stability diagram of a given steel composition. If T.Ca falls in the liquid window, the value of dimensionless Ca would be between 0 and 1. Dimensionless Ca larger than unity and being negative indicates that the T.Ca falls in the CaS stability region and CA_2 stability region, respectively.
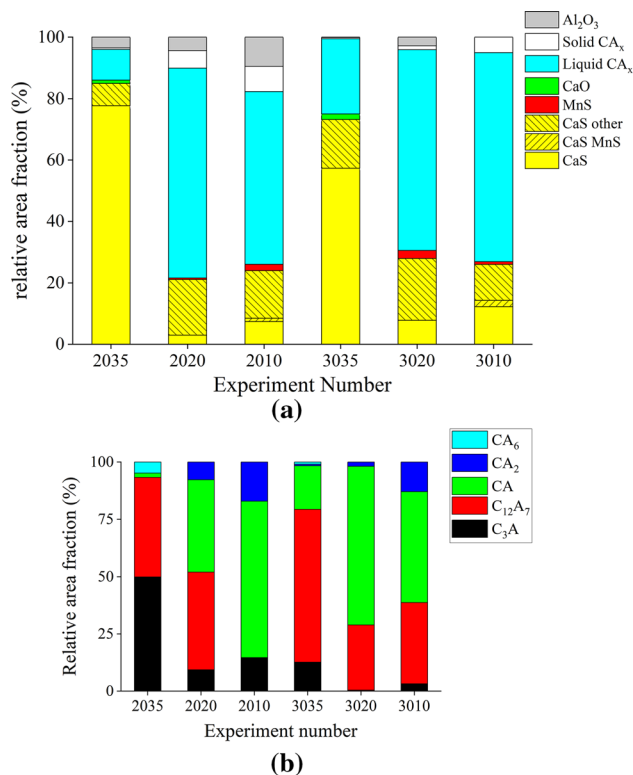
$$\text{dimensionless Ca} = \frac{(\text{T.Ca})_{\text{measured}} - (\text{T.Ca})_{\text{CA}_2 \text{ sat.}}}{(\text{T.Ca})_{\text{CaS sat.}} - (\text{T.Ca})_{\text{CA}_2 \text{ sat.}}} \quad [6]$$

$$\text{dimensionless Ca at 20 ppm T.O}$$
$$\approx \frac{\text{T.Ca} - 10.5}{1.128 \cdot \text{T.S}^{-0.406} \cdot \text{T.Al}^{-0.226} - 10.5} \quad [7]$$

$(\text{T.Ca})_{\text{CA}_2 \text{ sat.}}$ and $(\text{T.Ca})_{\text{CaS sat.}}$ values depend on T.O, T.S and T.Al contents of steel. These values for a value of T.O = 20 ppm are given in Eq. [7]. The developments of Eqs. [6] and [7] are included in the appendix. The three variables: T.Ca, T.S and T.Al used to calculate Eq. [7] can be obtained through typical online analysis, therefore, it is potentially suitable for process control in industrial practice.

The proposed parameter in Eq. [6] is validated against the obtained experimental results and industrial heats containing 20 ppm T.O. Figure 13 presents the calculated dimensionless Ca against the percentage of the AF of liquid CA_x (CA + $C_{12}A_7$ + C_3A) present in the 20 minutes sample of all the six experiments. Having a dimensionless Ca between 0 and 1, Exp. 2020, Exp. 3020 and Exp. 3010 showed the highest inclusion liquefaction. A dimensionless Ca value slightly below 0 (Exp. 2010) lead to an apparent drop in inclusion liquefaction. High dimensionless Ca values from Exp. 2035 and Exp. 3035 indicate that the measured Ca contents were in the CaS stability region and gave very low liquefaction due to the formation of CaS containing inclusions.

In addition to experimental steels, industrial heat data is also used to evaluate dimensionless Ca. Figure 14(a) shows the inclusion AF change in ladle during Ca injection and AF change in the tundish samples. This heat contains 0.05C–1Mn–0.23Si–0.03Al–0.003S (values are in wt pct). Figure 14(b) corresponds to a heat of 0.05C–1.2Mn–0.21Si–0.03Al–0.001S named Heat 2. The ladle samples were taken at different times after Ca injection was completed. The detailed sampling times as
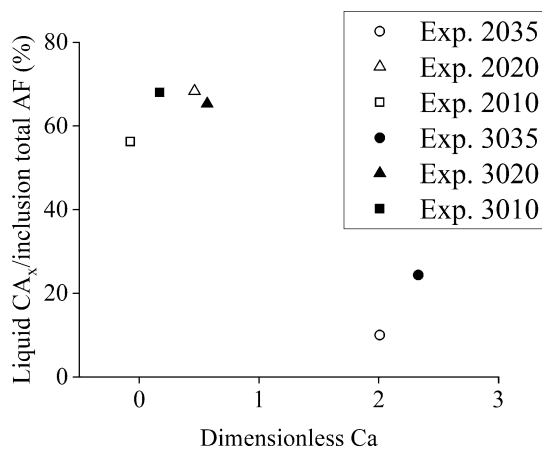
well as the temperatures are listed in Table II. Both heats were about 165 t. As seen in Figure 14, in both heats, the percentages of liquid CA_x were generally stable while CaS type inclusions increased over time. It is worth noticing that there was a sudden increase in the AF of CaS type inclusions in L3 of Heat 1 and keep increasing in the rest of the ladle and tundish samples. Although a similar phenomenon also appeared in Heat 2 starting L4, the increment in Heat 2 was no doubt much smaller.

By plotting the relative AF of liquid CA_x and that of solid CA_x and CaS type inclusions together against a change of dimensionless Ca, Figure 15 can be generated. Marks represent the relative AF, and solid lines show the evolution of dimensionless Ca. The dashed line indicates dimensionless Ca = 1 to improve visualization. During calcium addition in Heat 1, the dimensionless Ca increased from 0.32 to 2.16, and then decreased to 1.30 in the last tundish sample. It can be seen that, in the first two samples, when the dimensionless Ca was less than 1, the percentage of liquid CA_x is about 75 pct while the solid CA_x and CaS complexes were about 12 pct. MnS, spinel, and aluminate titanates also exist but were omitted because they are less than 8 pct of the total inclusion AF. As the dimensionless Ca exceeded unity, the percentage of CaS containing inclusions increased significantly, which is in line with what's shown in Figure 14. This resulted in a drastic reduction of inclusion liquefaction and agrees with the concept of introducing dimensionless Ca, as it correctly reflects the direction of inclusion liquefaction change. Although dimensionless Ca decreased in tundish samples, the steel composition would still be in the CaS stability region, hence the AF percentages of CaS complexes increased in the system. Similar trends were observed in the other heat shown in Figure 15(b). The percentage of liquid inclusions was high as about 80 pct in sample L1 of Heat 2 while dimensionless Ca was less than 1. As dimensionless Ca increased to 1.76 in L2 of Heat 2, the expected decrease in liquid CA_x percentage and increase in solid inclusion percentage can be observed. After that, the fraction of liquid CA_x and CaS complexes maintained a low value. The less significant liquefaction and CaS change in Heat 2 were potentially due to low S content. Interestingly, even after dimensionless Ca decreased to less than 1 (starting at sample L4), there was no significant variation in the percentage of liquid and solid inclusions.

Results shown in Figures 13 through 15 signify that there exists a strong correlation between the number of inclusions and dimensionless Ca. Hence, dimensionless Ca may be used to estimate the type of inclusions that will form if the evolution of the steel compositions is known. Moreover, due to simplicity of Eq. [6], dimensionless Ca can be applied on-line during the production process. More industrial heats will be studied in the future to confirm this finding.

The authors are aware that other means of estimating inclusion compositions, such as ratios of Ca/O and Ca/Al, have been proposed in the literature as reviewed in the introduction. The advantage of dimensionless Ca in
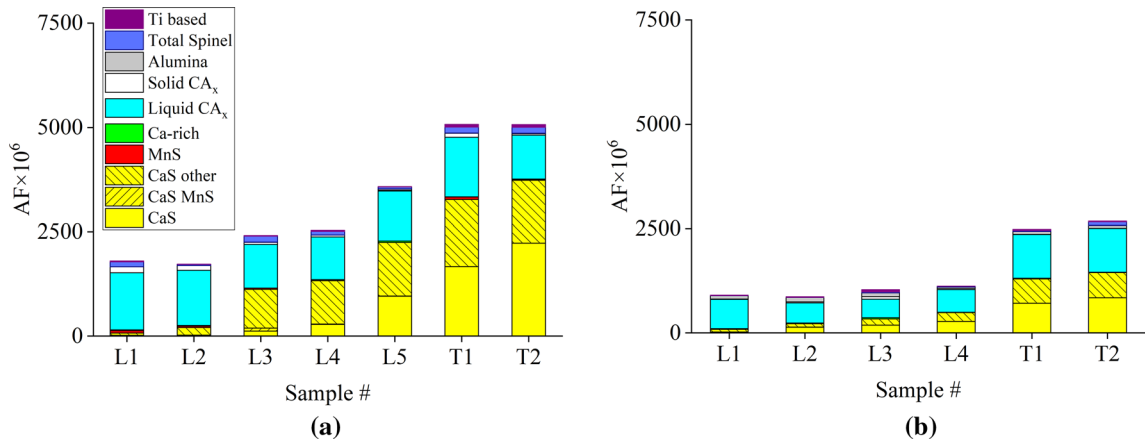

Fig. 13—The percentage of liquid CA_x dependency on dimensionless Ca in laboratory results.

Fig. 14—The AF of inclusions industrial heats (*a*) Heat 1 (*b*) Heat 2 (L and T represent ladle and tundish, respectively).

Table II. Detailed Sampling Time of Both Industrial Heats

|	Heat 1		Heat 2
Sample No	Sampling Time	Sample No	Sampling Time
L1	1.2 min after Ca injection start	L1	Ca injection complete
L2	2.2 min after Ca injection start	L2	1.5 min after completion
L3	3.2 min after Ca injection start	L3	4.1 min after completion
L4	4.3 min after Ca injection start	L4	6.3 min after completion
L5	4.7 min after Ca injection start (Ca injection complete)		
T1	80 t cast in Tundish	T1	80 t cast in Tundish
T2	125 t cast in Tundish	T2	125 t cast in Tundish
Temperature			
Ladle		1848K	
Tundish		1833K	
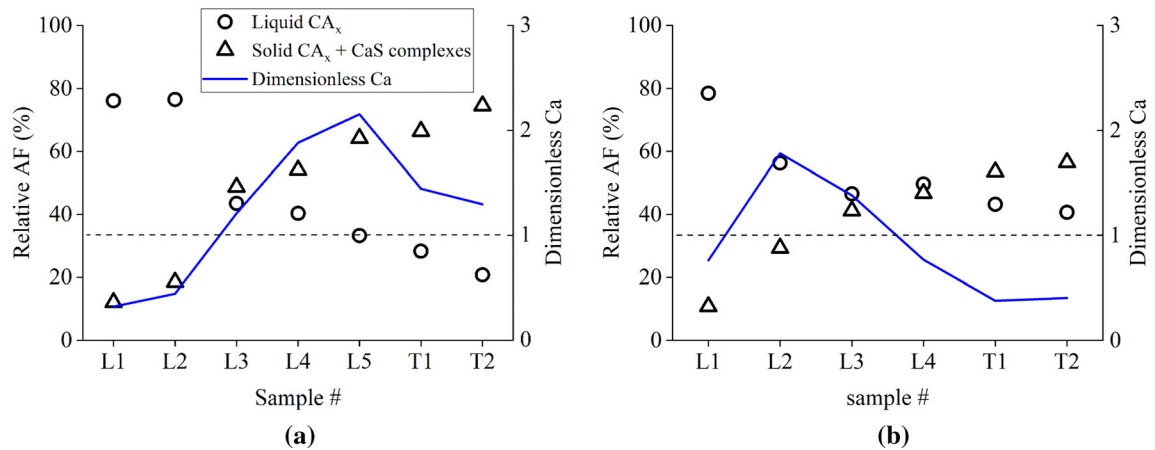
Fig. 15—The relative AF of inclusions with respect to dimensionless Ca for industrial heats (*a*) Heat 1 (*b*) Heat 2.

comparison to previously proposed correlations is that the calculation of dimensionless Ca includes all of the important variables: Al, S and Ca, hence can be adapted in a wide range of compositions with no important parameter omitted in the prediction. Second, the direct correlation between dimensionless Ca and the fraction of liquid inclusions makes dimensionless Ca more intuitive and accessible for practical uses.

VI. CONCLUSIONS

The effects of different amounts of Ca addition on the modification of inclusions were studied. The obtained results are summarized as follows:

1. The total amount of inclusions in steel depends on the amount of added Ca. In relatively high and low Ca conditions, the amount of CaS and liquid CA_x inclusions, which are, respectively, the thermodynamically stable inclusion types, increases with holding time.

2. Two inclusion modification mechanisms are observed in experiments. First, when the Ca contents are high in the melt, CaO can be observed. Then as Ca content decreases, CaO transforms to CaS. Subsequently, Al_2O_3 inclusions are modified by CaS to CA_x. The second mechanism is when the added Ca is insufficient to form CaO. In this case, Al_2O_3 inclusions are initially modified by [Ca] then by CaS. In this case, CaS inclusions are the product of [Ca] and [S] reaction.

3. A new parameter, 'dimensionless Ca' is proposed in this study, which can be used to predict the extent of modification of inclusions based upon the measured Ca content of the steel. A value of dimensionless Ca between 0 and 1 suggests higher liquefaction of inclusions, whereas dimensionless Ca greater than one predicts liquefaction drop due to the increase in CaS containing inclusions. This is validated against industrial heat data.

APPENDIX: SIMPLIFICATION OF DIMENSIONLESS CA CALCULATION

Dimensionless Ca in theory can be calculated of any known chemistry. In practise, its value can be approximated for a fixed T.O. Figure A1 shows the change of inclusion stability with respect to the steel chemistry. Similar graphs for different conditions can be found in the References 8,16,32, and 33. The region where steel chemistry falls in the "liquid CA_x" region is referred to as the liquid window, and high inclusion liquefaction can be observed.

As shown in Figure A1, the upper and lower T.Ca limits of the liquid window can be determined by the Equilibrium [A1] and [A2], respectively.
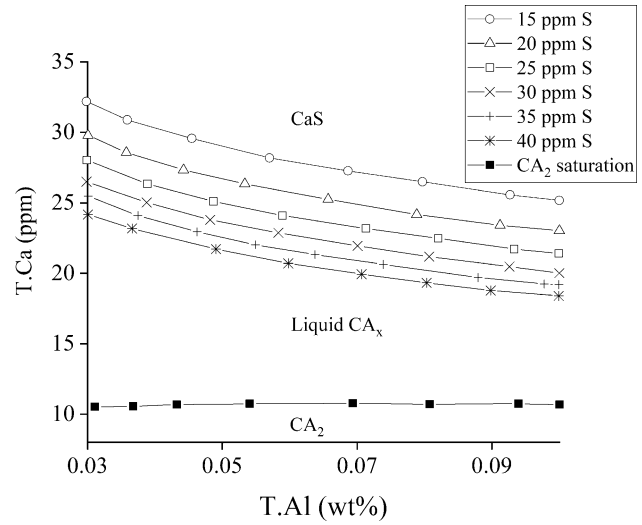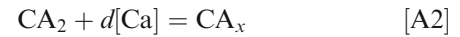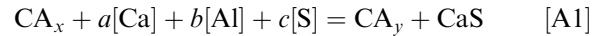

Fig. A1—The upper limit and lower limit T.Ca of the liquid window were calculated in FactSage assuming 20 ppm T.O and experimental temperature of 1873 K.

$$CA_x + a[Ca] + b[Al] + c[S] = CA_y + CaS \qquad [A1]$$

$$CA_2 + d[Ca] = CA_x \qquad [A2]$$

For Equilibrium [A1], there must exist Eq. [A3], which can be converted to Eq. [A4].

$$\Delta G = -RT \ln\left(\frac{1}{h_{Ca}^a h_{Al}^b h_{S}^c}\right) \qquad [A3]$$

$$h_{Ca} = \exp\left(\frac{\Delta G}{aRT}\right) \cdot h_{Al}^{-\frac{b}{a}} h_{S}^{-\frac{c}{a}} \qquad [A4]$$

C, Si, and Mn mostly dissolve in the liquid steel, so T.C ≈ [C], T.Si ≈ [Si], T.Mn ≈ [Mn]. Taking steel with composition of 0.06C–0.25Si–1Mn (all in wt pct) as an example, the Al activity coefficient can be represented with Eq. [A5] where e_j^i and [i] are the interaction coefficient and mass fraction of component i. The interaction coefficients used can be found in the References 10 and 34. The [Ca] and [O] have low concentrations; hence they can be omitted in the calculation of the Al activity coefficient. If the steel contains 20 ppm T.O and all O exists in the form of Al_2O_3, this will only account for 23 ppm of Al, which is still about one order of magnitude lower than typical T.Al in Al-killed steels. Hence, it is considered T.Al ≈ [Al] is a valid assumption in most of the cases. Taking the industrial heats from ArcelorMittal Dofasco as an example, the maximum T.Al = 0.082 wt pct. And at the upper limit of the liquid window, the amount of CaS formed will be very small, so T.S ≈ [S]. Maximum T.S = 278 ppm in the industrial heats. Either using simultaneously the maximum T.Al and T.S or minimum T.Al and T.S give $\log f_{Al}$ ranges

from 0.026 to 0.03, which means always $f_{Al} \approx 1$. Therefore, $h_{Al} \approx [Al] \approx$ T.Al in Eq. [A4]. Following the same logic, $h_S \approx [S] \approx$ T.S.

$$\log f_{Al} = \sum_i e_{Al}^i [i] = 0.026 + 0.045[Al] + 0.03[S] \quad [A5]$$

So far the author cannot find a simply correlated between Ca activity and T.Ca. It is therefore assumed:

$$h_{Ca} = k \cdot \text{T.Ca} \quad [A6]$$

where $0 < k \ll 1$. Substitute all activities to Eq. [A4], we have

$$\begin{aligned} \text{T.Ca} &= \frac{1}{k} \exp\left(\frac{\Delta G}{aRT}\right) \cdot \text{T.Al}^{-\frac{b}{a}} \cdot \text{T.S}^{-\frac{c}{a}} \\ &\approx A \cdot \text{T.S}^{-j} \cdot \text{T.Al}^{-i} \end{aligned} \quad [A7]$$

Assuming $\frac{1}{k}\exp\left(\frac{\Delta G}{aRT}\right) = A$ is a constant (need to be improved in the future) and fit the upper limit T.Ca of the liquid windows at various S levels shown in Figure A1 into a series of power function of T.Al, we get the equations listed in Table A1. Comparing equations in Table A1 and Eq. [A7], clearly the factor B satisfies $B = A \cdot \text{T.S}^{-j}$. Plotting B against S level in Figure A2, gives a fitted function $y = 1.128x^{-0.406}$. Using the average of parameter i in Table A1 for Eq. [A7], we get:

$$\text{T.Ca} = 1.128 \cdot \text{T.S}^{-0.406} \cdot \text{T.Al}^{-0.226} \quad [A8]$$

Validating the fitted function [A8] against FactSage calculated upper limit T.Ca of the liquid window from 20 ppm to 80 ppm T.S, the error of T.Ca was ±4 pct. This can be used to calculate dimensionless Ca using Eq. [A9]. Constant 10.5 is the T.Ca lower limit of the liquid window, which has negligible dependence on S and Al contents. Equation [A8] does not incorporate the effect of other elements in steel because their effects on the liquid window are found to be insignificant within the interested steel composition ranges at 1873 K.

The purpose of Eq. [A9] is to provide a quick and more accessible approximation of dimensionless Ca for practical use, although it can only be applicable for a limited range of steel chemistries at the current stage of research.

$$\begin{aligned} &\text{dimensionless Ca at 20 ppm T.O} \\ &\approx \frac{\text{T.Ca} - 10.5}{1.128 \cdot \text{T.S}^{-0.406} \cdot \text{T.Al}^{-0.226} - 10.5} \end{aligned} \quad [A9]$$

Table A1. Excel Fitted Power Functions for the Upper Limit T.Ca of the Liquid Window

T.S (ppm)	Fitted Function T.Ca = $B \cdot$ T.Al^{-i}	R^2
15	T.Ca = $15.892 \cdot$ T.Al$^{-0.201}$	0.9993
20	T.Ca = $14.061 \cdot$ T.Al$^{-0.214}$	0.9994
25	T.Ca = $12.896 \cdot$ T.Al$^{-0.221}$	0.9992
30	T.Ca = $11.866 \cdot$ T.Al$^{-0.230}$	0.9989
35	T.Ca = $11.143 \cdot$ T.Al$^{-0.235}$	0.9996
40	T.Ca = $10.824 \cdot$ T.Al$^{-0.230}$	0.9996
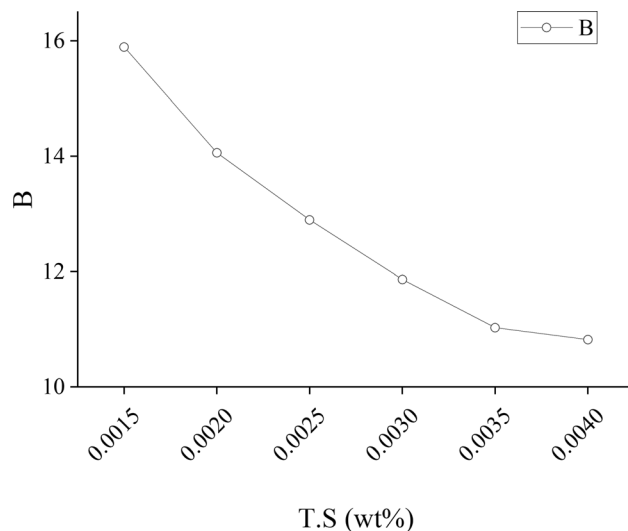
Fig. A2—The dependency of parameter B on T.S.

REFERENCES

1. S. Sun, S. Waterfall, N. Strobl, D. Liao, and D. Holdridge: *Miner. Met. Mater. Ser.*, 2017, vol. PartF5, pp. 347–57.
2. E.T. Turkdogan: *Fundamentals of Steelmaking*, The Institute of Materials, London, 1996.
3. W. Yang, L.F. Zhang, X. Wang, Y. Ren, X. Liu, and Q. Shan: *ISIJ Int.*, 2013, vol. 53, pp. 1401–10.
4. N. Verma, P.C. Pistorius, R.J. Fruehan, M.S. Potter, H.G. Oltmann, and E.B. Pretorius: *Metall. Mater. Trans. B*, 2012, vol. 43B, pp. 830–40.
5. K. Yang, S., Zhang, L., Sun, L., Li, J., and Peaslee: *AISTech 2011 Proc.*.
6. S.F. Yang, J.S. Li, Z.F. Wang, J. Li, and L. Lin: *Int. J. Miner. Metall. Mater.*, 2011, vol. 18, pp. 18–23.
7. D. Zhao, H. Li, C. Bao, and J. Yang: *ISIJ Int.*, 2015, vol. 55, pp. 2115–24.
8. S.K. Choudhary and A. Ghosh: *ISIJ Int.*, 2008, vol. 48, pp. 1552–59.
9. G. Yang and X. Wang: *ISIJ Int.*, 2015, vol. 55, pp. 126–33.
10. J. Xu, F. Huang, and X. Wang: *Metall. Mater. Trans. B*, 2016, vol. 47B, pp. 1217–27.
11. Z. Deng and M. Zhu: *Steel Res. Int.*, 2013, vol. 84, pp. 519–25.
12. G.M. Faulring, J.W. Farrell, and D.C. Hilty: *Ironmak. Steelmak.*, 1980, vol. 7, pp. 14–20.
13. S. Yang, Q. Wang, L. Zhang, J. Li, and K. Peaslee: *Metall. Mater. Trans. B*, 2012, vol. 43B, pp. 731–50.
14. J.H. Park, D.S. Kim, and S.B. Lee: *Metall. Mater. Trans. B*, 2005, vol. 36B, pp. 67–73.
15. D. Lu: McMaster University, 1992.
16. L. Holappa, M. Hämäläinen, M. Liukkonen, and M. Lind: *Ironmak. Steelmak.*, 2003, vol. 30, pp. 111–15.
17. Y. Tabatabaei, K.S. Coley, G.A. Irons, and S. Sun: *Metall. Mater. Trans. B*, 2018, vol. 49B, pp. 375–87.
18. Y. Tabatabaei, K.S. Coley, G.A. Irons, and S. Sun: *Metall. Mater. Trans.*, 2018, vol. 49B, pp. 2022–37.
19. M. Lind and L. Holappa: *Metall. Mater. Trans. B*, 2010, vol. 41B, pp. 359–66.
20. N. Verma, P.C. Pistorius, R.J. Fruehan, M. Potter, M. Lind, and S.R. Story: *Metall. Mater. Trans. B.*, 2011, vol. 42B, pp. 720–29.
21. Y. Liu, L. Zhang, Y. Zhang, H. Duan, Y. Ren, and W. Yang: *Metall. Mater. Trans. B*, 2018, vol. 49B, pp. 610–26.

22. Z.J. Han, L. Liu, M. Lind, and L. Holappa: *Acta Metall. Sin. (English Lett.)*, 2006, vol. 19, pp. 1–8.
23. Y. Ito, M. Suda, Y. Kato, H. Nakato, and K. Sorimachi: *ISIJ Int.*, 1996, vol. 36, pp. S148–50.
24. M.K. Sardar, S. Mukhopadhyay, U.K. Bandopadhyay, and S.K. Dhua: *Steel Res. Int.*, 2007, vol. 78, pp. 136–40.
25. J.M.A. Geldenhuis and P.C. Pistorius: *Ironmak. Steelmak.*, 2000, vol. 27, pp. 442–49.
26. Y. Ren, L.F. Zhang, and S. Li: *ISIJ Int.*, 2014, vol. 54, pp. 2772–79.
27. V. Gollapalli, M.B.V. Rao, P.S. Karamched, C.R. Borra, G.G. Roy, and P. Srirangam: *Ironmak. Steelmak.*, 2018, vol. 36, pp. 432–41.
28. X. Wang, X. Li, Q. Li, F. Huang, H. Li, and J. Yang: *Steel Res. Int.*, 2014, vol. 85, pp. 155–63.
29. Y. Higuchi, M. Numata, S. Fukagawa, and K. Shinme: *ISIJ Int.*, 1996, vol. 36, pp. S151–54.
30. N. Verma, P.C. Pistorius, R.J. Fruehan, M. Potter, M. Lind, and S. Story: *Metall. Mater. Trans. B*, 2011, vol. 42B, pp. 711–19.
31. S. Sun, L. Sun, S. Waterfall, D. Liao, A.G. R, D. Hamilton, and S. Technology: vol. 2, pp. 1–18.
32. S. Wang, J. Zhang, R. Cheng, and H. Ma: *Trans. Indian Inst. Met.*, 2018, vol. 71, pp. 2231–42.
33. W.V. Bielefeldt and A.C.F. Vilela: *Steel Res. Int.*, 2015, vol. 86, pp. 375–85.
34. Japan Society for the Promotion of Science: *Steelmaking Data Sourcebook*, Gordon and Breach Science Publishers, New York, 1988.